



ARTICLE

A Method for Ultrasound Servo Tracking of Puncture Needle

Shitong Ye¹, Bo Yang^{2,*}, Hao Quan³, Shan Liu⁴, Minyi Tang⁵ and Jiawei Tian^{6,*}

¹School of Artificial Intelligence, Guangzhou Huashang College, Guangzhou, 511300, China

²School of Automation, University of Electronic Science and Technology of China, Chengdu, 610054, China

³Department of Electronics, Information and Bioengineering (DEIB), Politecnico di Milano, Via Ponzio 34/5, Milan, 20133, Italy

⁴Department of Modelling, Simulation, and Visualization Engineering, Old Dominion University, Norfolk, VA 23529, USA

⁵Graduate School of Engineering, ESIGELEC, Av. Galilée, St Etienne du Rouvray, 76801, France

⁶Department of Computer Science and Engineering, Hanyang University, Ansan, 15577, Republic of Korea

*Corresponding Authors: Bo Yang. Email: boyang@uestc.edu.cn; Jiawei Tian. Email: tianjiawei@hanyang.ac.kr

Received: 01 April 2025; Accepted: 19 June 2025; Published: 31 August 2025

ABSTRACT: Computer-aided surgical navigation technology helps and guides doctors to complete the operation smoothly, which simulates the whole surgical environment with computer technology, and then visualizes the whole operation link in three dimensions. At present, common image-guided surgical techniques such as computed tomography (CT) and X-ray imaging (X-ray) will cause radiation damage to the human body during the imaging process. To address this, we propose a novel Extended Kalman filter-based model that tracks the puncture needle-point using an ultrasound probe. To address the limitations of Kalman filtering methods based on position and velocity, our method of Kalman filtering uses the position and relative velocity of the puncture needle-point instead, and the ultrasonic probe is controlled by a Proportional Integral (PI) controller in X-axis direction and Proportional Derivative (PD) controller in the Y-axis direction. The motion of the ultrasonic probe can be servo-controlled by whether the image information of the puncture needle-point can be detected by the ultrasonic image so that the ultrasonic probe can track the puncture needle-point in real time. The experiment results show that this method has better tracking performance.

KEYWORDS: Surgical navigation system; ultrasonic image; servo control; position and relative velocity; extended Kalman filtering

1 Introduction

Computer-assisted surgical systems encompass a confluence of interdisciplinary domains including computer science, information management, communication technology, mechanics, and image processing [1–5]. Their principal objective resides in the emulation of the comprehensive surgical milieu through computer technologies, thereby guiding and supporting surgeons in the successful execution of surgical procedures. Foremost among these systems is image-guided surgery [6], an emerging technique in minimally invasive medical interventions that leverages multimodal medical imaging to facilitate preoperative surgical path planning. This entails real-time imaging modalities like ultrasound imaging, necessitating the integration of tracking and localization apparatus during surgical procedures to ascertain the spatial coordinates and orientations of surgical probes and lesions. The resultant real-time spatial data is then co-registered with preoperative images, presenting a virtual amalgamation within the same coordinate framework. This virtual alignment furnishes surgeons with real-time navigational insights, enhancing tasks such as the precise placement of surgical probes to minimize collateral damage.



Ultrasound (US) imaging, grounded in ultrasound wave propagation, acquires internal organ images by processing the reflected signals obtained through scanning the human body [7,8]. This pioneering effort materialized in clinical settings, signifying the maturation of ultrasound-based navigation for clinical practice. Notably, in contemporary minimally invasive procedures like radiofrequency ablation and biopsy surgeries [9], two-dimensional ultrasound images supplant other imaging modalities such as CT scans, mitigating radiation exposure while delivering real-time intraoperative visuals. Nevertheless, the utility of two-dimensional ultrasound is hindered by volumetric limitations that engender imprecise target localization and varying procedural risks.

In numerous minimally invasive medical interventions, the introduction of needles into tissue constitutes a crucial diagnostic and treatment modality. The accuracy of needle tip placement critically underpins procedural success. Deviations in needle tip positioning can engender misdiagnosis (e.g., biopsy) or hinder effective treatment (e.g., radiotherapy) [10,11]. Imaging-guided needle insertion relies on techniques encompassing computed tomography (CT) scans, fluoroscopy, magnetic resonance imaging (MRI), and ultrasound imaging. The deployment of CT, however, is marred by heightened ionizing radiation exposure for patients [12]. Furthermore, CT-guided interventions are limited to instruments fabricated from non-magnetic and dielectric materials [13]. In contrast, ultrasound stands as a benign and easily accessible imaging modality, facilitating real-time visualization of needles and target lesions during surgical procedures [14,15].

Presently, the efficacy of two-dimensional ultrasound imagery falters in the accurate delineation of spatial lesion data, often succumbing to partial volume artifacts [16]. These artifacts arise due to the concurrent visualization of echoes from adjacent tissues anterior and posterior to the lesion within the same image. Consequently, these extraneous echoes interfere with the unobstructed observation of the lesion, thereby engendering partial volume artifacts [17] within two-dimensional ultrasound scans. Five primary methodologies are discernible for needle tracking: signal and image processing techniques, sensor calibration, manipulation of ultrasound image formation, motion analysis-driven approaches, and machine learning-based methodologies [18]. Moreover, the domain of real-time servo tracking of flexible needle tips using ultrasound imaging remains underexplored [19,20], with prevailing research primarily concentrated on the tracking of rigid needle tips [21,22].

Addressing this, Baker et al. formulated a real-time ultrasound needle tracking system [23] to avert untoward incidents due to misplaced needle tips, exhibiting commendable accuracy. Conventional methods encompass the localization and tracking of needle tips through ultrasound image filtration [24–26]. In a similar vein, Mathews et al. proffered a technique for needle tip tracking via integration of fiber-optic ultrasound sensors within the needle cannula [27], substantiating tracking precision through clinical training models. In contrast, ultrasound probes are encumbered in their capacity to capture needle tip movements extending beyond the two-dimensional plane.

Recent work has begun to harness deep learning to overcome the low-contrast, noise-rich nature of ultrasound (US) guidance. Che et al. [28] integrated a Siamese correlation-filter network with optical navigation data, letting the optical tracker both constrain the search window and retrospectively correct outliers; the hybrid system reduced mean tip-localisation error to roughly 1 mm in phantom punctures. Hui et al. [29] introduced UIU-Net, a network trained with photo-acoustic images as automatic ground truth, thereby avoiding manual annotation and achieving sub-millimetre segmentation accuracy in *ex vivo* tissue and promising transfer to *in vivo* human data. Complementing these vision-centric strategies, Yan et al. [30] fused a transformer-based motion-prediction module with a visual tracker, boosting robustness when the tip

temporarily disappears in gelatin or biological tissue inserts. These studies demonstrate the power of data-driven models but still depend on sizeable, annotated datasets, additional sensing hardware, or significant computational overhead.

To address the above issues, we propose an improved ultrasound servo-tracking scheme for flexible needle navigation based on an Extended Kalman Filter (EKF). The classical Proportional Integral (PI) controller is used for the X -axis speed control, for which a dynamic reference speed adjustment strategy is specially designed to improve the tracking performance of the X -axis. The Y -axis position control uses a PD controller to ensure that the needle tip is always in the center position of the ultrasound image. The results show that the proposed method has superior tracking performance compared to the existing method.

2 Method

In this section, we introduce the method using a two-dimensional ultrasound probe for three-dimensional tracking of the needle tip. Firstly, we propose a controller for locating the ultrasound probe. Then, we calculate the coordinates of the tip of the puncture needle in a fixed coordinate system [22,23]. Finally, once the image information of the puncture needle is detected by the ultrasonic image, it is used to servo-control the movement of the probe. As illustrated in Fig. 1, the ultrasonic probe can track the tip of the puncture needle in real time.

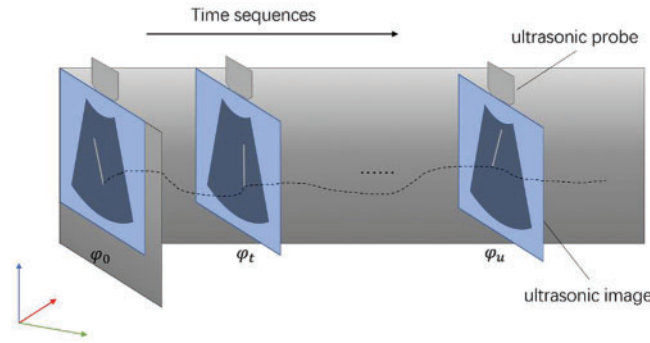


Figure 1: Pipeline of puncture needle's tip tracking based on ultrasound images

2.1 Motion Modeling of Puncture Needle Tip

The robotic arm drives the puncture needle into the soft-tissue phantom ψ_0 along the phantom's X -axis at velocity v . Meanwhile, the arm keeps the ultrasound image plane moving parallel to this X -axis. The first ultrasound frame captured after the needle enters the tissue is designated as the yOz -plane of a fixed reference frame; using the right-hand rule, this frame also establishes the positive X -axis direction. All subsequent calculations in the experiment are carried out within this fixed coordinate system.

Under this system, the coordinate value of needle's tip is defined as Eq. (1):

$$P = [p_x, p_y, p_z]^T \quad (1)$$

where p_x, p_y, p_z are the positions of the needle tip on the x -axis, y -axis, and z -axis, respectively.

Its velocity is the derivative of position vs. time t and is defined as in Eq. (2):

$$V = [v_x, v_y, v_z]^T \quad (2)$$

where v_x, v_y, v_z are the speeds of the needle tip on the x -axis, y -axis, and z -axis, respectively.

Let v_{in} be the feed speed of the flexible needle given by the insertion device. The relationship between the feed speed and the velocity of the needle tip is shown as Eq. (3):

$$v_{in} = \|V\|_2 \quad (3)$$

where $\|*\|_2$ represents the L2 norm.

2.2 Principle of Ultrasonic Servo

The compensator is used to move the ultrasound probe along the X -axis according to the needle tip velocity. The estimated error of P_x will lead to the positioning error of the ultrasound probe along the x -axis (frame (ψ_0)). Positioning error is defined as in Eq. (4):

$$\delta = |P_x - P_u| \quad (4)$$

where P_u is position of ultrasonic probe. δ is the absolute error of the ultrasound image along the X -axis (ψ_0), the pixel deviation of the ultrasound image. δ illustrates the pose error of the needle's tip in the total calculated pose between frames ψ_t and ψ_u .

The calculated pose of the needle's tip is defined as H_0^u . By applying closed-loop control, reduce the pixel error of the ultrasound image and the pose error. From the ultrasound image, it is possible to determine whether the tip is in or out of plane. Therefore, it is possible to control the ultrasonic transducer along the x -axis (ψ_0) in a closed loop by adjusting the speed gain K_e and velocity v_u . When the needle is in the plane or outside the plane, K_e is used to increase ($K_e = 1.05$) or decrease ($K_e = 0.5$) the speed of the ultrasonic probe.

By using a gain controller to change the speed of the ultrasonic probe, the ultrasonic probe is forced to move towards the needle's tip and minimize δ . Thus, it is possible to calculate the pose of the needle tip H_0^u . There are two cases for the speed of the sensor that controls the ultrasound image: first case, the ultrasound image does not detect the puncture needle. The ultrasound image is in front of the puncture needle in this case, set K_e to 0.5, and the ultrasound image will move slowly to approach the needle's tip. Second case, the ultrasound image can detect the puncture needle, set K_e to 1.05, and the ultrasound image accelerates to approach the tip. Finally, the ultrasonic image will move around the tip to achieve the purpose of ultrasound image servo control of the tip movement.

2.3 Model of Servo-Motor-Driven Robotic Arm

The motion model of servo-motor-driven manipulator can be simplified as a damper and a mass model as shown in Fig. 2, and the mechanical equation is defined as Eq. (5):

$$f = ma + bv \quad (5)$$

where a is the acceleration of the mass, b is the damping coefficient of the damper, v is the velocity of the mass, m is the mass of the mass, f is the external force on the mass.

While controller synthesis adopts a lumped mass–damper representation, the ensuing phantom experiments employ the physical robot, so friction, backlash, and compliance are implicitly contained in all experiments' reports.

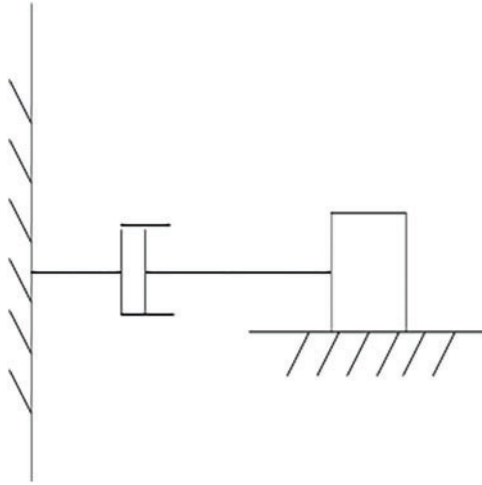


Figure 2: Model of ultrasonic servo drive

2.4 State Equations of the Extended Kalman Filter

Since the 2D ultrasound only detects targets within the 2D scanning plane and has large measurement noise, in this work, the EKF is used to estimate the 3D position and velocity of the tip from the noisy and intermittent measurements provided by the 2D ultrasound system. Two different forms of state vectors are designed for the EKF.

2.4.1 Position and Velocity State Vector

The Position and Velocity (PV) state vector is composed of the 3D position of the needle tip and its velocity components, $v_{yz} = [v_y, v_z]^T$, in the Y and Z directions, represented by Eq. (6):

$$\mathbf{x} = \begin{bmatrix} P \\ v_{yz} \end{bmatrix} \quad (6)$$

The classical Constant Velocity (CV) model is used to construct the state equation for needle tip motion, as shown in Eq. (7):

$$\begin{cases} p(k+1) = p(k) + v(k) + w_p(k) \\ v_{yz}(k+1) = v_{yz}(k) + w_v(k) \end{cases} \quad (7)$$

where k denotes the k -th sampling moment, $w_{p/v}$ is the processing noise of the position/velocity component.

The derivative of Eq. (7) with respect to the state vector \mathbf{x} yields the linearized state transition matrix $A(k)$, as shown in Eq. (8):

$$A(k) = \begin{bmatrix} 1 & 0 & 0 & -v_y(k)/v_x(k) & -v_z(k)/v_x(k) \\ 0 & 1 & 0 & 1 & 0 \\ 0 & 0 & 1 & 0 & 1 \\ 0 & 0 & 0 & 1 & 0 \\ 0 & 0 & 0 & 0 & 1 \end{bmatrix} \quad (8)$$

where $v_x(k) = \sqrt{v_{in}^2(k) - v_y^2(k) - v_z^2(k)}$ can be obtained from Eq. (3).

Let z be the 3D measurement of the tip position derived from the ultrasound system. The measurement equation is written as Eq. (9):

$$z(k) = Hx(k) + v(k) \quad (9)$$

where v is the measurement noise, H is the constant measurement matrix, written as Eq. (10):

$$H = \begin{bmatrix} 1 & 0 & 0 & 0 \\ 0 & 1 & 0 & 0 \\ 0 & 0 & 1 & 0 \end{bmatrix} \quad (10)$$

2.4.2 Position and Relative Velocity State Vector

Due to the use of the classical CV model, the PV state model will inevitably receive a shock when there is an abrupt change in the needle feed speed. To solve this issue, the relative velocity concerning v_{in} is introduced into the state vector, as shown in Eq. (11):

$$\mathbf{x} = \begin{bmatrix} P \\ v'_{yz} \end{bmatrix} \quad (11)$$

where $v'_{yz} = [v'_y, v'_z]^T$ with $v'_{y,z} = v_{y,z}/v_{in}$ being the relative velocity components.

The state equation still uses the CV model defined in Eq. (7). With the Position and Relative Velocity (PRV) state vector defined by Eq. (11), the state transition matrix is defined as in Eq. (12):

$$A(k) = \begin{bmatrix} 1 & 0 & 0 & -v'_y(k)/v'_x(k) & -v'_z(k)/v'_x(k) \\ 0 & 1 & 0 & 1/v_{in}(k) & 0 \\ 0 & 0 & 1 & 0 & 1/v_{in}(k) \\ 0 & 0 & 0 & 1 & 0 \\ 0 & 0 & 0 & 0 & 1 \end{bmatrix} \quad (12)$$

where $v'_x = \sqrt{1 - v'^2_y - v'^2_z}$, derived from Eq. (3).

The measurement equation is consistent with that of the PV case (see Eq. (9)).

2.5 Phantom Experiment Setup

All experiments in this study were carried out on a water-bath tissue-mimicking phantom using the actual ultrasound probe, EC63 collaborative robot, and industrial camera, listed in Table 1.

Table 1: Phantom experiment device

Device	Manufacturer/Model
Ultrasound probe	SonoStar (Guangzhou, China), a full-digital diagnostic system, CProbe
Collaborative robot	Elite Robots (Knoxville, TN, USA), EC63 (6-DoF, modular, lightweight)
Industrial camera	MindVision (Shenzhen, China), MV-MSU130GM2-T

In the experiment, the camera, robotic arm, and industrial camera are all commercial products with clear manufacturers and models. The calibration plates of the ultrasound probe and puncture needle are generated by 3D printing, and each calibration plate is equipped with four optical balls. The actual experimental environment and some components are shown in Fig. 3:

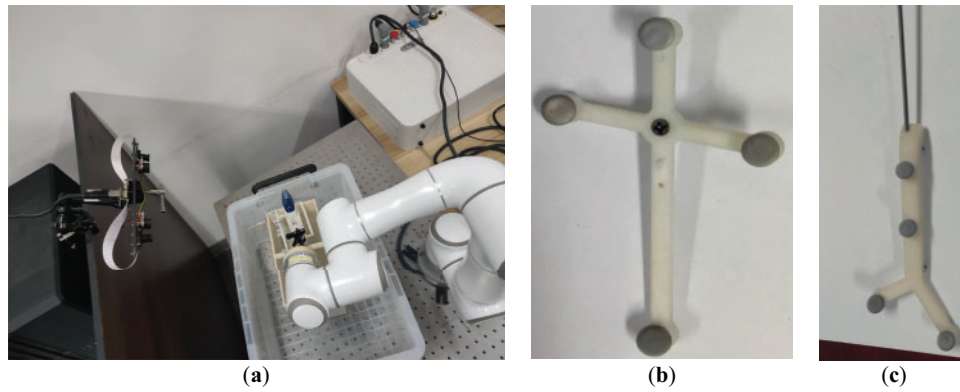


Figure 3: Schematic diagram of the experimental equipment. (a) Experimental scene; (b) Ultrasonic probe optical calibration plate; (c) Puncture needle tip optical calibration plate

3 Controller Design for Controlling Ultrasound Probes

The Kalman filter [31] employed in this study follows the standard two-stage workflow of prediction and correction. The controller calculates the control variable (f in Eq. (5)) for the manipulator based on the state estimates of the needle tip from the EKF and the current position and velocity feedback of the ultrasound probe from the manipulator's encoder.

As shown in Fig. 4, the Y-direction tip position estimated by the EKF is denoted as \hat{p}_y , and the X-direction velocity estimate is denoted as \hat{v}_x , which can be derived from the Y- and Z-direction velocity estimates of the EKF using Eq. (3). In the X-direction, a PI controller is used to control the velocity of the ultrasound probe, where the reference (desired) velocity is obtained by multiplying the EKF's velocity estimate \hat{v}_x by a proportional gain K_e . In the Y direction, a PD controller is used to control the position of the ultrasound probe, where the reference (desired) position is the EKF's position estimate \hat{p}_y .

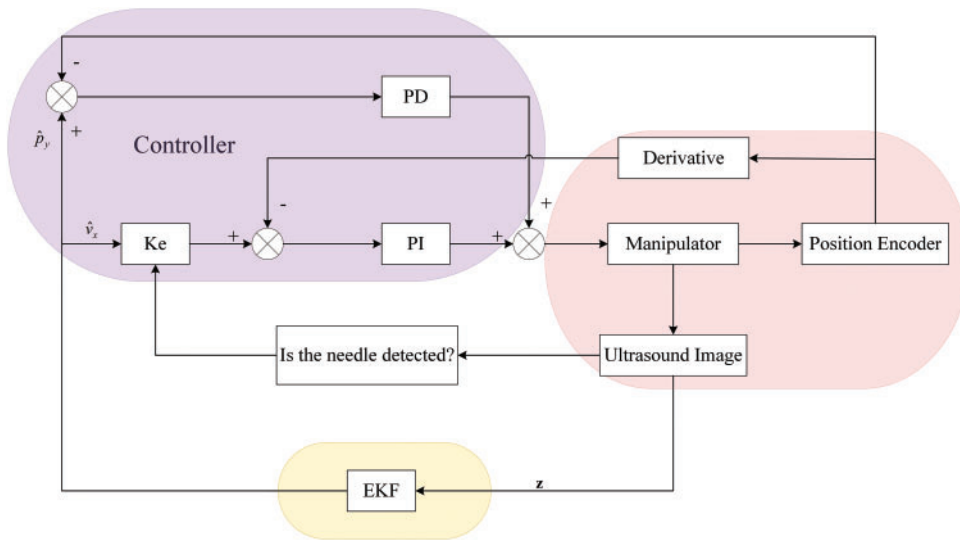


Figure 4: Overall control block diagram for tracking the needle tip using 2D ultrasound images

3.1 Controller in the X-Axis Direction

In the proportional derivative (PD) controller [32], the proportional component reacts proportionally to system deviations. Higher proportional gains accelerate adjustment and reduce errors; however, excessively high gains may compromise system stability, potentially causing instability. The integral component eliminates steady-state errors and enhances error correction, which integrates the speed error over time until the error is eliminated. Once the velocity deviation is zero (the feedback velocity is equal to the reference velocity), the integral component ensures that the controller outputs a constant f to maintain this velocity balance.

As shown in Fig. 5, the reference velocity is obtained by multiplying the X-direction velocity estimate \hat{v}_x by the gain K_e . The gain K_e will determine whether the ultrasound probe is moving at a velocity above or below the estimated velocity of the needle tip. When the needle is not detected in the ultrasound image, it means that the scanning plane is ahead of the needle tip, and the ultrasound probe should move at a speed lower than that of the needle (i.e., $K_e < 1$), on the contrary, it means that the scanning plane lags behind the needle tip, and the ultrasound probe should move at a speed higher than the needle (i.e., $K_e > 1$).

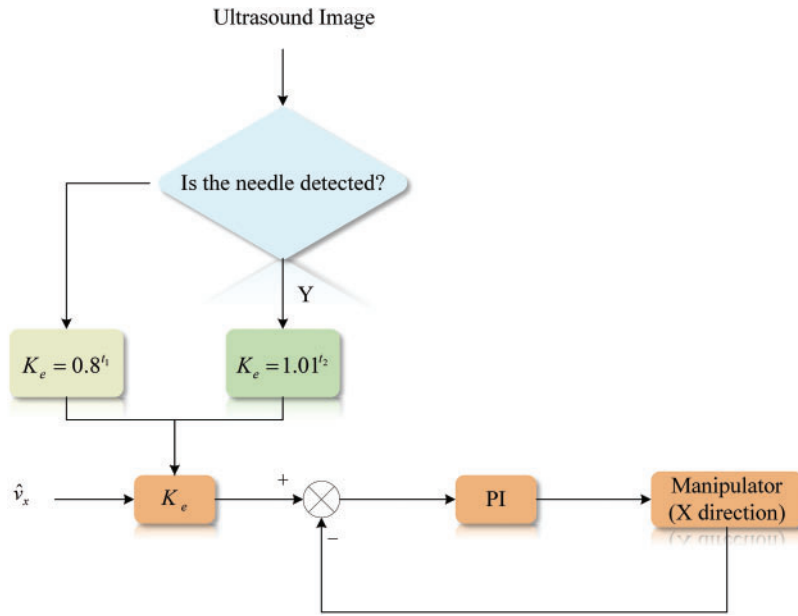


Figure 5: Control flow graph for X-axis direction

To achieve this, a dynamic speed regulation strategy is designed as Eq. (13):

$$K_e = \begin{cases} 0.8^{t_1}, & \text{if needle is not detected} \\ 1.01^{t_2}, & \text{if needle is detected} \end{cases} \quad (13)$$

where t_1 and t_2 are the number of consecutive frames in which the needle is not detected/is detected in the ultrasound images. With Eq. (13), the speed of the ultrasound probe in the X direction will decay exponentially if the needle is detected for multiple consecutive frames, and conversely, the speed will increase exponentially if the needle is detected for multiple consecutive frames.

The velocity difference at the k -th control cycle is first calculated by Eq. (14):

$$e_x(k) = K_e \hat{v}_x(k) - v_{ux}(k-1) \quad (14)$$

where $K_e \hat{v}_x(k)$ is the reference velocity, $v_{ux}(k-1)$ is the actual velocity of the ultrasound probe obtained from the manipulator's encode after the previous cycle of controlling. By inputting $e_x(k)$ into the PI controller and taking the output into Eq. (5), it can be obtained as Eq. (15):

$$K_{p1}e_x(k) + K_i \sum_{i=1}^k e_x(i) = ma_{ux}(k) + bv_{ux}(k) \quad (15)$$

where K_{p1} is the coefficient of the proportional element, K_i is the coefficient of the integral element, and $a_{ux}(k) = v_{ux}(k) - v_{ux}(k-1)$ is the acceleration of the ultrasound probe.

Solving Eq. (15) gives the velocity of the ultrasound probe after the k -th control cycle, as shown in Eq. (16):

$$v_{ux}(k) = \frac{K_{p1}e_x(k) + K_i \sum_{i=1}^k e_x(i) + mv_{ux}(k-1)}{m+b} \quad (16)$$

3.2 Controller in the Y-Axis Direction

The standard proportional derivative (PD) controller is used to control the movement of the ultrasound probe along the Y direction, so that the needle is always centered in the Y -axis of the ultrasound image. The proportional term amplifies the magnitude of the error and improves the response of the system, while the differential term predicts the trend of the error change and reduces overshooting. As illustrated in Fig. 6.

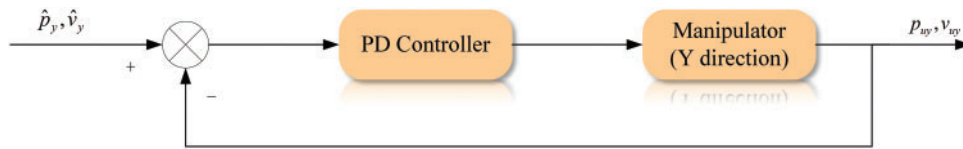


Figure 6: Control flow graph for Y-axis direction

The position difference is first calculated: as Eq. (17):

$$e_y(k) = \hat{p}_y(k) - p_{uy}(k-1) \quad (17)$$

where $\hat{p}_y(k)$ is the reference position estimated by the EKF, and $p_{uy}(k-1)$ is the Y -coordinate of the ultrasound probe after the previous cycle of controlling. The process of the PD controller adjusting the error can be expressed as Eq. (18):

$$K_{p2}e_y(k) + K_D[e_y(k) - e_y(k-1)] = ma_{uy}(k) + bv_{uy}(k) \quad (18)$$

where K_{p2} represents the coefficient of the proportional element, and K_D represents the coefficient of the differential element. a_{uy} and v_{uy} denote the actual acceleration and velocity of the ultrasound probe in the Y direction, respectively.

The Y coordinate of the ultrasound probe after the k -th control cycle is derived by Eq. (19):

$$p_{uy}(k) = p_{uy}(k-1) + \frac{K_{p2}e_y(k) + (m - K_D)v_{uy}(k-1)}{m+b} \quad (19)$$

4 Experiments

4.1 Experiment Setup

The proposed servo tracking scheme is validated based on a simulated puncture trajectory. The frame rate (sampling frequency) of the ultrasonic system is set to $f_u = 25$ Hz, which is also the filtering frequency of the EKF. The operating frequency of the discrete PI and PD controllers is set to 7500 Hz, which means that the controllers will perform $f_p/f_u = 300$ closed-loop adjustments with a constant reference value (\hat{v}_x or \hat{v}_y) estimated by the EKF, during each sampling period of the ultrasound image.

The velocities of the puncture needle are planned with the sampling frequency f_u . As shown in Fig. 7, the insertion velocity v_{in} is uniformly accelerated from 0 to 2 mm/s for the first 100 samples, remains constant for the next 400 samples, jumps to 3 mm/s at the 500th samples, remains constant again for the next 1000 samples, and jumps back to 2 mm/s at the 1500th samples until the end of the 2000th samples.

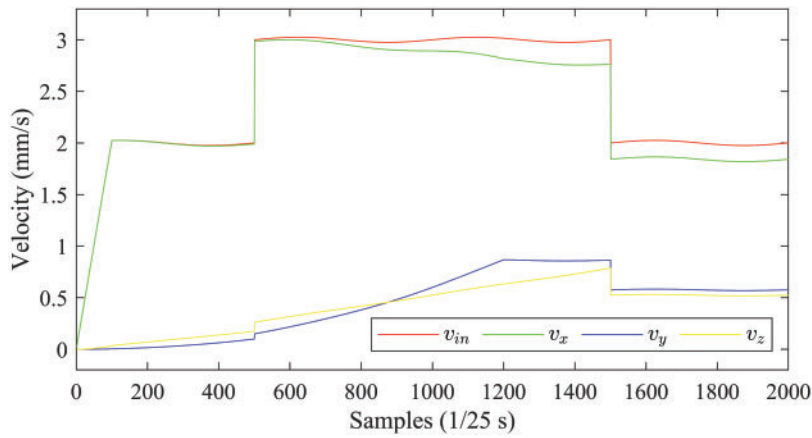


Figure 7: Planned velocity curves of the needle tip

To simulate the dynamic perturbation of the insertion device, a sinusoidal component with an amplitude of 0.025 mm/s and a period of 20 s is superimposed on the above planned velocity profile.

According to Eq. (3), the insertion velocity v_{in} is dynamically decomposed into three velocity components $\{v_x, v_y, v_z\}$.

In Fig. 7, the velocity components $\{v_y, v_z\}$ tend to increase, meaning that the puncture needle, initially parallel to the X axis, gradually bends in the positive direction of the Y and Z axes.

Without loss of generality, the starting point of the needle trajectory is at the origin of the world coordinate system. The whole trajectory of the needle tip is shown in Fig. 8.

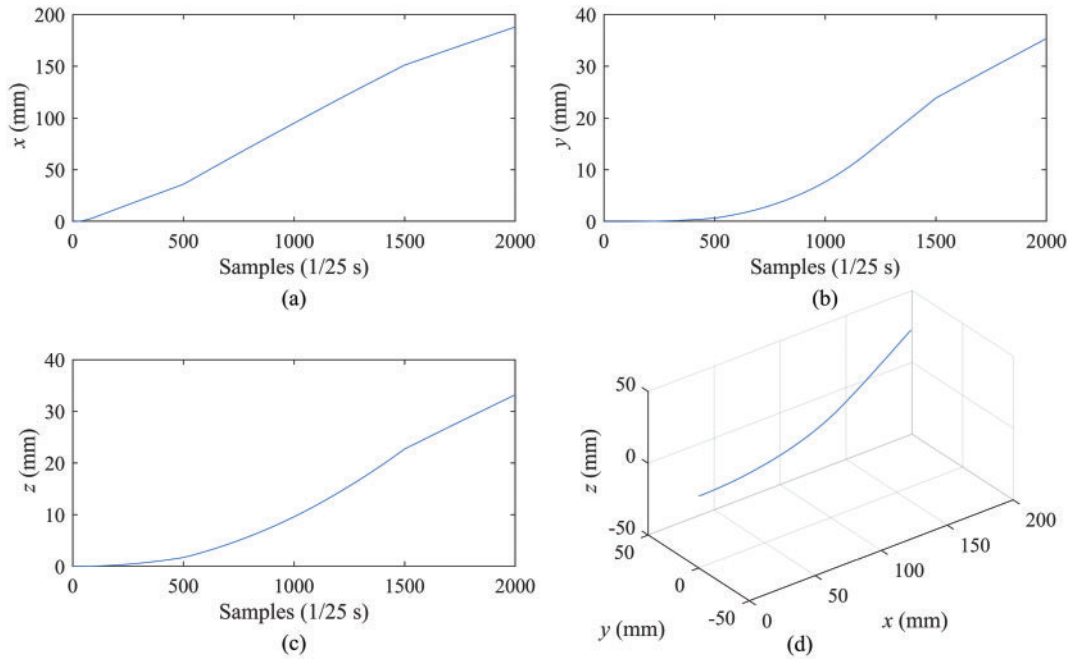


Figure 8: Simulation of needle tip motion. (a–c) are the moving curves of the needle tip in the X, Y, and Z axes, respectively. (d) is the 3D trajectory of the needle tip

From Fig. 8d, it is observed that the 3D trajectory of the tip is smooth and shows a continuous direction change during the puncture, which is consistent with the actual puncture process. In Fig. 8a–c, the motion curves of the tip exhibits dynamics consistent with the insertion speed (v_{in}) in all three directions, where the inflection points at the 500th and 1500th samples correspond to the step changes in the insertion speed.

The parameters of the manipulator model are set as follows: the mass $m = 150$ and the damping coefficient $b = 20$. The PI controller in the X direction is set to $K_{p1} = 100$, $K_i = 20$, and the PD controller in the Y direction is set to: $K_{p2} = 30$, $K_D = 50$.

4.2 Phantom Experiment Based on Position and Velocity (PV)

The covariance matrix of processing noise used in the EKF is set as Eq. (20):

$$Q_{PV} = \begin{bmatrix} 10^{-6} & 0 & 0 & 0 & 0 \\ 0 & 10^{-6} & 0 & 0 & 0 \\ 0 & 0 & 10^{-6} & 0 & 0 \\ 0 & 0 & 0 & 5 \times 10^{-6} & 0 \\ 0 & 0 & 0 & 0 & 5 \times 10^{-6} \end{bmatrix} \quad (20)$$

And the covariance matrix of measurement noise is set to Eq. (21):

$$R_{PV} = \begin{bmatrix} 0.5 & 0 & 0 \\ 0 & 100 & 0 \\ 0 & 0 & 100 \end{bmatrix} \quad (21)$$

where the variances in the Y and Z directions are significantly larger than those in the X direction because a large measurement noise (uniformly distributed from -2 to 2 mm) is added to the ideal detected values of the ultrasound images to simulate real ultrasound imaging.

The results of needle tip tracking in the Y direction are shown in Fig. 9. The measurement of the needle tip in the Y direction, denoted by z_y in the figure, is generated by adding noise to the ideal measurement.

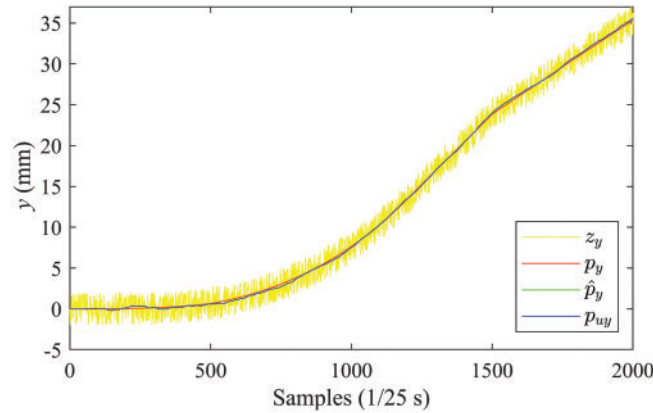


Figure 9: Position curves in the Y -direction (PV)

It can be observed from the figure that the EKF can effectively suppress the noise measurement in ultrasound devices. The estimated \hat{p}_y is very close to the true value p_y , and using the PD controller, the ultrasonic probe can be accurately tracking the movement of the needle tip in the Y direction.

Tracking in the X direction is further complicated by the need to control the ultrasound probe to alternate imaging in front of and behind the tip. Fig. 10 shows the results in the X direction.

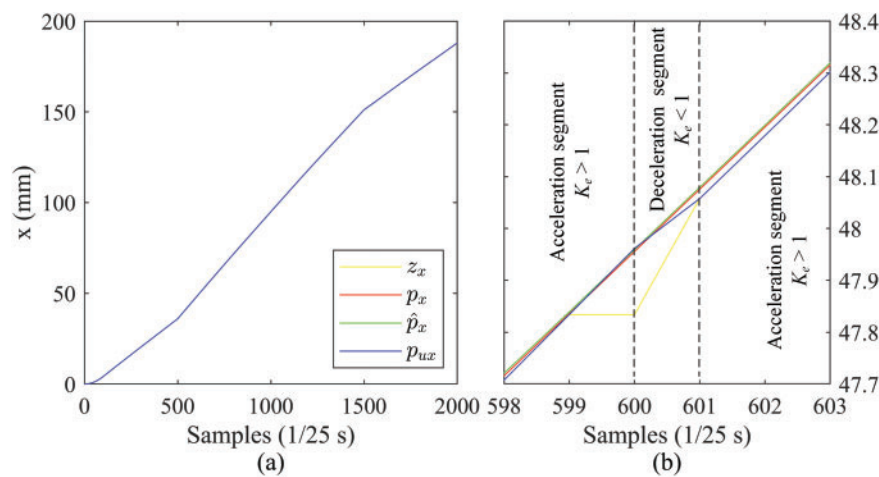


Figure 10: Position curves in the X direction (PV): (a) complete curves, (b) zoomed-in details

The tracking accuracy in the X direction is quite high. To illustrate the details of the tracking, the curves from samples 598 to 603 are zoomed in. As can be seen from the zoomed-in graph, in the several samples before 600, the ultrasound scanning plane is behind the needle tip, and the X direction motor accelerates to catch up. At the sample 600, the ultrasound probe has caught up with the tip, at which time the needle

cannot be detected in the ultrasound image, so the measurement z_x at sample 600 copies the value at the previous sample (599). It is also at the sample 600 that K_e . Subsequently, at sample 601, the ultrasound probe again succeeded in capturing the needle and went into the acceleration segment.

With this switching of acceleration and deceleration controlled by K_e , the ultrasound probe can chase the needle tip in the X direction. As shown in Fig. 10, the p_{ux} curve sometimes exceeds the true curve p_x and sometimes lags it. Moreover, the proposed tracking scheme enables the needle to be visible in the ultrasound image at most sampling moments, representing a safe control strategy. In addition, the EKF still shines in the X direction, though the measurement of the tip in the X direction is unreliable, which is taken directly from the position of the ultrasound probe and can be blocked.

Fig. 11 shows the velocity curves in the X and Y directions estimated by the EKF with the PV state vector.

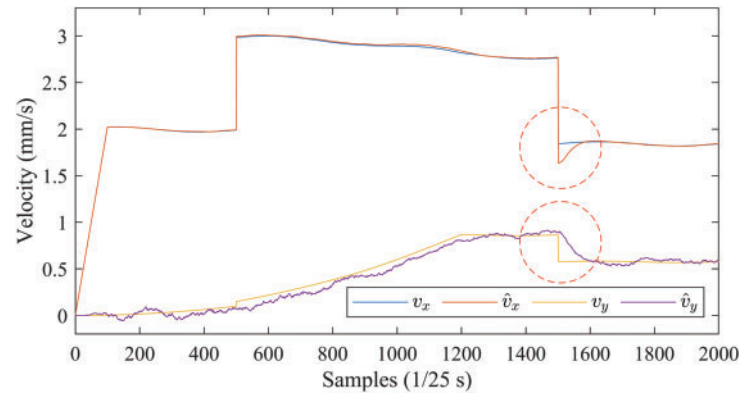


Figure 11: Velocity curves in the X and Y directions estimated by EKF (PV)

The velocity estimates are generally accurate, and only when the insertion speed changes abruptly are there short transitions (marked by red circles) in the estimated curves ($\hat{v}_{x/y}$), which briefly deviate from their true curves but quickly revert.

Fig. 12 shows the 3D motion trajectories of the needle tip estimated by the EKF with the PV state vector.

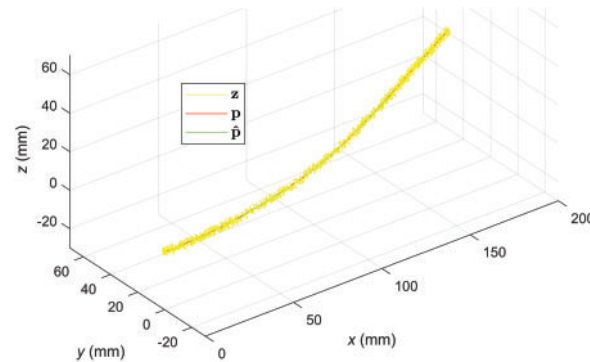


Figure 12: Velocity curves in the X and Y directions estimated by EKF (PV)

Despite the large noise in the measurements (z), the estimated trajectory (\hat{p}) overlaps almost exactly with the true trajectory (p), indicating that the proposed scheme can accurately track the motion of the needle tip.

4.3 Phantom Experiment with PRV State Vector

The covariance matrix of processing noise for the PRV case is set as in Eq. (22):

$$Q_{PRV} = \begin{bmatrix} 5 \times 10^{-6} & 0 & 0 & 0 & 0 \\ 0 & 10^{-6} & 0 & 0 & 0 \\ 0 & 0 & 10^{-6} & 0 & 0 \\ 0 & 0 & 0 & 5 \times 10^{-6} & 0 \\ 0 & 0 & 0 & 0 & 5 \times 10^{-6} \end{bmatrix} \quad (22)$$

And the covariance matrix of measurement noise is set to Eq. (23):

$$R_{PRV} = \begin{bmatrix} 0.5 & 0 & 0 \\ 0 & 100 & 0 \\ 0 & 0 & 100 \end{bmatrix} \quad (23)$$

The tracking results in the Y and X directions are shown in Figs. 13 and 14, respectively. Similar to the results in Figs. 9 and 10, both the estimates of the EKF ($\hat{p}_{y/x}$) and the positions of the ultrasound probe ($p_{uy/ux}$) are very close to the true values ($p_{y/x}$), indicating that the EKF with the PRV state vector is effective.

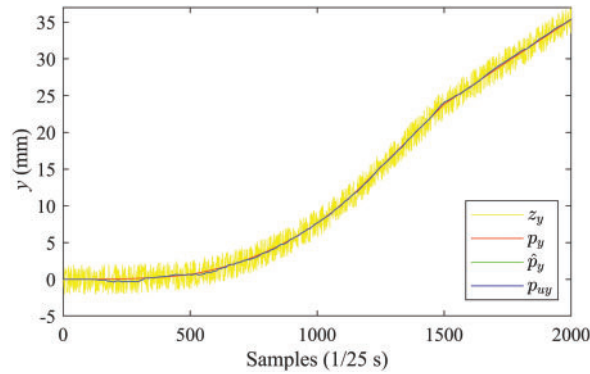


Figure 13: Position curves in the Y direction (PRV)

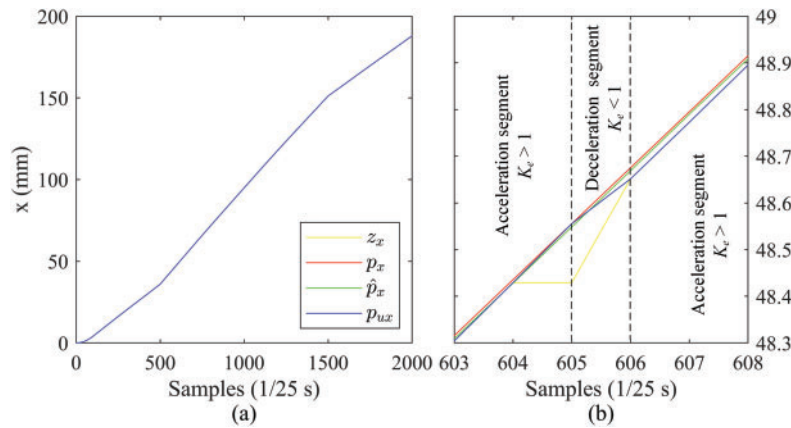


Figure 14: Position curves in the X direction (PRV): (a) complete curves, (b) zoomed-in details

Fig. 15 shows the velocity curves in the X and Y directions estimated by the EKF with the PRV state vector.

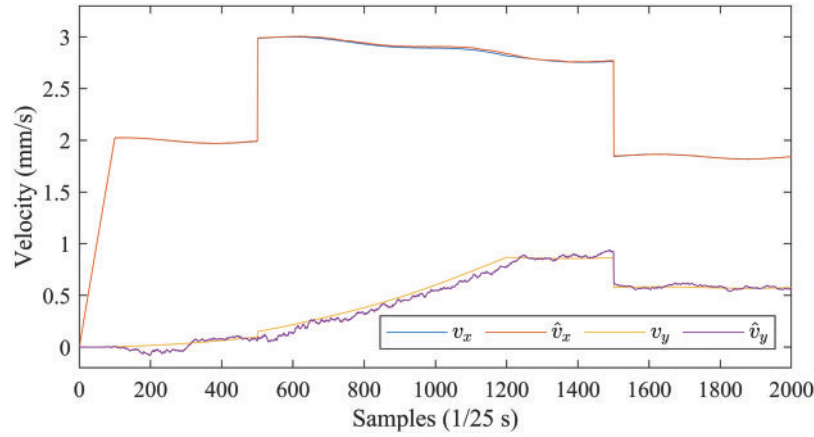


Figure 15: Velocity curves in the X and Y directions estimated by EKF (PRV)

Comparison with Fig. 11 shows that the EKF with PRV can effectively cope with the perturbations caused by sudden changes in insertion speed, with consistently accurate velocity estimates in all directions.

The effectiveness of the EKF with PRV is also demonstrated by the 3D motion trajectories in Fig. 16.

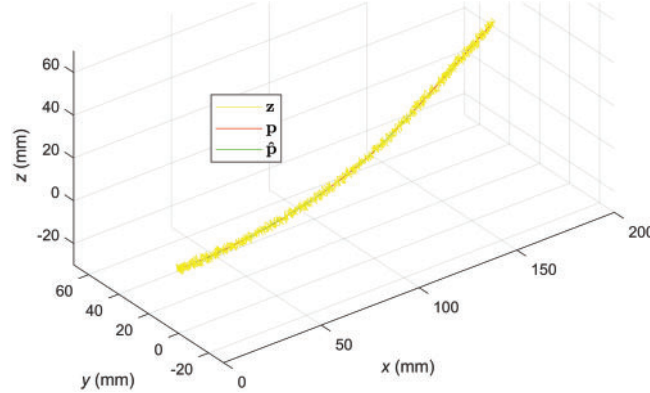


Figure 16: 3D motion trajectories of the needle tip estimated by the EKF (PRV)

4.4 Quantitative Evaluation

The proposed tracking scheme is quantitatively compared with a baseline scheme proposed in [33] (labelled by ICRA since it is published in ICRA 2013), in which K_e was set to constants (1.05 and 0.5, respectively) depending on whether the needle was detected in the ultrasound image.

Table 2 shows the average Root Mean Square Errors (RMSE) obtained through 100 repetitions of the experiment using our scheme and the ICRA benchmark with PR and PRV as state vectors, respectively. The first two rows of the table show the estimated errors of the 3D position and X direction velocity of the EKF, compared to the true values of the tip. The third and fourth rows show the position control errors of the ultrasound probe in the X and Y directions, respectively, compared to the true value of the tip.

Table 2: Average RMSE for 100 repetitions of the simulation

RMES	Ours (PRV)	ICRA (PRV)	Ours (PV)	ICRA (PV)
\hat{P} vs. P (mm)	0.1803	0.1858	0.1898	0.1950
\hat{v}_x vs. v_x (mm)	0.0076	0.0075	0.0247	0.0277
p_{ux} vs. p_x (mm)	0.0113	0.0266	0.0122	0.0353
p_{uy} vs. p_y (mm)	0.1225	0.1227	0.1337	0.1357
Lead-lag ration	0.176	0.101	0.073	0.097

In both PRV and PV configurations, our scheme achieves lower RMSEs than the ICRA benchmark. In particular, the position control accuracy in the X direction (see the row of p_{ux} vs. p_x in the table) is significantly better than the ICRA benchmark, indicating that our scheme allows the ultrasound probe to follow the tip more closely.

The comparisons between PRV and PV are consistent with those between Figs. 11 and 15, and both show that the introduction of relative velocity components in the state vector improves the estimation accuracy of the EKF, and the enhancement is significant, especially in the estimation of velocity in the X direction. The last row of 15 in the table shows the Lead-Lag Ratio between the ultrasound probe and the needle tip, which indicates that all methods allow the ultrasound probe to be located behind the tip most of the time, resulting in valid measurements.

5 Discussion

This study introduces a needle tip tracking technique utilizing ultrasound images, primarily concentrating on motion-centric approaches for needle localization [34]. This method facilitates servo-driven manipulation of the ultrasound probe contingent on the needle tip's image-derived information. We propose two distinct approaches: one rooted in position and velocity, and the other in position and relative velocity.

In terms of the final positional tracking accuracy, there is little difference in the performance of the PV and PRV-based EKFs, both of which can accurately localize and track the tip motion, with the PRV slightly outperforming the PV. While in terms of velocity estimation, the PRV is significantly better than the PV, especially when there are step changes in the insertion speed, the PRV performs robustly and can insulate the state estimation from the sudden changes of the insertion speed. Unlike the binary constant velocity control strategy proposed in [33], our strategy dynamically adjusts the reference velocity of the X -direction PI controller according to the number of consecutive ultrasound frames in which the needle is detected or not detected, thus enhancing its adaptability and tracking accuracy. The phantom experiment results demonstrate the effectiveness of this dynamic velocity strategy.

For the six-degree-of-freedom robotic arm featured in this study, the adoption of a conventional Proportional Integral Derivative (PID) control algorithm exhibits the potential to ameliorate the end effector's positional accuracy within the XY plane. Building upon the conclusions drawn in this article, we independently employ PI and PD controllers along the x -axis and y -axis orientations. This strategic integration aims to mitigate discrepancies in the velocity's deviation signals following Kalman filtering and the needle tip's velocity, thereby enhancing overall control precision.

Although this study concentrates on tip-tracking accuracy, it is important to recognize that the phantom experiments inherently incorporate a range of real-world uncertainties. The water-bath setup introduces ultrasound speckle and intensity shading, while the Elite EC63 robot contributes joint friction, minor backlash, and compliance. In addition, slight probe-pressure fluctuations were induced by gentle agitation

of the water surface during each run. These factors collectively represent the types of disturbances expected in a clinical environment. In the proposed position and relative velocity Kalman framework, we mitigate the effects of these uncertainties in three ways. First, the noise covariance process is adjusted online by monitoring the innovation sequence; this maintains the filter's responsiveness without overreacting to transient speckle bursts or instantaneous probe drift. Second, innovations in measurements are discarded if they exceed a preset innovation covariance multiple, thus suppressing the effects of sudden illumination changes. Finally, the controller gains are determined through a series of benchtop experiments that vary the insertion speed and probe trajectory. The consistent tracking performance in these experiments shows that modest parameter changes do not destabilize the closed-loop system.

While our motion-centered, position-and-relative velocity Kalman framework provides accurate needle tip tracking with modest computational demands, we acknowledge that the current study has significant limitations. All results were obtained on a water bath simulated tissue phantom. Although this setup exposes the system to realistic mechanical and imaging perturbations, it cannot capture acoustic heterogeneity and physiological motion *in vitro* or *in vivo* experiments. Therefore, this study should be viewed as a "theory plus phantom" feasibility test and not a substitute for clinical evidence. This study has not yet been clinically tested, and the safety aspects are still under discussion. Before clinical deployment, the system must meet the following requirements. For the control part of the instrument arm, the probe contact pressure needs to be limited to avoid tissue damage beyond the range. And provide fail-safe protection when the ultrasound image quality degrades or the tracking is lost. The above issues can be solved by additional multi-sensor solutions [35], such as combining ultrasound with electromagnetic tracking, probe-mounted inertial measurement units (IMUs), and wrist force sensing. This approach can not only improve robustness but also provide redundant safety prompts, triggering automatic pause or retraction actions when the threshold is exceeded.

6 Conclusion

Three-dimensional motion tracking of a flexible puncture needle using a 2D ultrasound system is a challenging task. Conventional closed-loop position control cannot be used due to the limited capability of the 2D ultrasound as a sensor for measuring the position of the needle tip, whose sensing field is a very thin plane. To achieve tip tracking, the servo control system must accurately drive the ultrasound probe to alternate images in front of and behind the tip based on noisy and discontinuous measurements provided by the ultrasound images. The proposed tracking scheme uses EKF to estimate the position and velocity of the tip from noisy and incomplete measurements. Two different forms of state vectors are investigated in the EKF: one based on position and velocity and the other on position and relative velocity. Based on the state estimation of EKF, the PI and PD controllers are used for velocity control in X direction and position control in Y direction, respectively. A dynamic velocity control strategy is designed in the X direction based on whether the needle is detected in the ultrasound images. Finally, we validate the proposed scheme in a simulation and compare it with a benchmark scheme. Phantom experiment results demonstrate the effectiveness and advantages of the proposed scheme.

Subsequent endeavors could incorporate a mechanical arm designed to govern the xOy plane probe's rotation, ensuring the ultrasound image maintains alignment with the normal line perpendicular to the needle tip's trajectory. This configuration would ensure that the ultrasound probe's X -axis velocity corresponds to the X -axis component of its velocity. This refinement would reduce X -axis displacement, subsequently enhancing tracking performance.

Furthermore, the current experimental setup wherein the ultrasonic probe is affixed to move solely along the X -axis direction introduces scenarios where the puncture needle tip's image might elude detection

in the ultrasound image. Prospective work envisions an ultrasound image that continuously tracks the puncture needle tip along the tangent direction of its trajectory, thereby enabling real-time puncture needle tip tracking.

Acknowledgement: Not applicable.

Funding Statement: The research was supported by the Sichuan Science and Technology Program (2023YFSY0026, 2023YFH0004).

Author Contributions: The authors confirm contribution to the paper as follows: Conceptualization, Bo Yang and Hao Quan; methodology, Minyi Tang; software, Shitong Ye; validation, Bo Yang, Jiawei Tian and Shan Liu; formal analysis, Hao Quan; investigation, Shitong Ye; resources, Minyi Tang; data curation, Shan Liu; writing—original draft preparation, Shitong Ye; writing—review and editing, Jiawei Tian; visualization, Jiawei Tian; supervision, Minyi Tang; project administration, Shan Liu; funding acquisition, Bo Yang, Shan Liu and Hao Quan. All authors reviewed the results and approved the final version of the manuscript.

Availability of Data and Materials: Experimentdata and source code are publicly available (<https://github.com/Caroline1-W/Tracking-of-Puncture-Needle>, accessed on 18 June 2025).

Ethics Approval: Not applicable.

Conflicts of Interest: The authors declare no conflicts of interest to report regarding the present study.

References

1. Chen YW, Hanak BW, Yang TC, Wilson TA, Hsia JM, Walsh HE, et al. Computer-assisted surgery in medical and dental applications. *Expert Rev Med Devices*. 2021;18(7):669–96. doi:10.1080/17434440.2021.1886075.
2. Chen Y, Xu L, Chen H, Zeng Y, Guo S, Deng J, et al. Two-stage and two-discriminator generative adversarial network for the inpainting of irregularly incomplete iris images. *Displays*. 2024;82:102626. doi:10.1016/j.displa.2023.102626.
3. Hu W, Jin T, Pan Z, Xu H, Yu L, Chen T, et al. An interpretable ensemble learning model facilitates early risk stratification of ischemic stroke in intensive care unit: development and external validation of ICU-ISPM. *Comput Biol Med*. 2023;166:107577. doi:10.1016/j.compbimed.2023.107577.
4. Zhang H, Cai Z, Xiao L, Heidari AA, Chen H, Zhao D, et al. Face image segmentation using boosted grey wolf optimizer. *Biomimetics*. 2023;8(6):484. doi:10.3390/biomimetics8060484.
5. Graf T, Keul C, Wismeijer D, Güth JF. Time and costs related to computer-assisted versus non-computer-assisted implant planning and surgery. A systematic review. *Clin Oral Implants Res*. 2021;32(Suppl 21):303–17. doi:10.1111/clr.13862.
6. Li H, Kim D, Yao Q, Ge H, Chung J, Fan J, et al. Activity-based NIR enzyme fluorescent probes for the diagnosis of tumors and image-guided surgery. *Angew Chem Int Ed*. 2021;60(32):17268–89. doi:10.1002/anie.202009796.
7. Xia J, Chen H, Li Q, Zhou M, Chen L, Cai Z, et al. Ultrasound-based differentiation of malignant and benign thyroid Nodules: an extreme learning machine approach. *Comput Methods Programs Biomed*. 2017;147(7):37–49. doi:10.1016/j.cmpb.2017.06.005.
8. Avola D, Cinque L, Fagioli A, Foresti G, Mecca A. Ultrasound medical imaging techniques. *ACM Comput Surv*. 2022;54(3):1–38. doi:10.1145/3447243.
9. Xiao J, Zhang Y, Zhang M, Lan Y, Yan L, Luo Y, et al. Ultrasonography-guided radiofrequency ablation vs. surgery for the treatment of solitary T1bN0M0 papillary thyroid carcinoma: a comparative study. *Clin Endocrinol*. 2021;94(4):684–91. doi:10.1111/cen.14361.
10. Youk JH, Kim EK, Kim MJ, Lee JY, Oh KK. Missed breast cancers at US-guided core needle biopsy: how to reduce them. *Radiographics*. 2007;27(1):79–94. doi:10.1148/rg.271065029.

11. Li P, Yang Z, Jiang S. Needle-tissue interactive mechanism and steering control in image-guided robot-assisted minimally invasive surgery: a review. *Med Biol Eng Comput*. 2018;56(6):931–49. doi:10.1007/s11517-018-1825-0.
12. Fred HL. Drawbacks and limitations of computed tomography: views from a medical educator. *Tex Heart Inst J*. 2004;31(4):345–8.
13. Fischer GS, Iordachita I, Csoma C, Tokuda J, DiMaio SP, Tempany CM, et al. MRI-compatible pneumatic robot for transperineal prostate needle placement. *IEEE/ASME Trans Mechatron*. 2008;13(3):295–305. doi:10.1109/TMECH.2008.924044.
14. Shulman SG, March DE. Ultrasound-guided breast interventions: accuracy of biopsy techniques and applications in patient management. *Semin Ultrasound CT MR*. 2006;27(4):298–307. doi:10.1053/j.sult.2006.05.004.
15. Wu YC, Chen DR, Kuo SJ. Personal experience of ultrasound-guided 14-gauge core biopsy of breast tumor. *Eur J Surg Oncol*. 2006;32(7):715–8. doi:10.1016/j.ejso.2006.04.012.
16. Wu X, Niu Z, Xu Z, Jiang Y, Zhang Y, Meng H, et al. Fetal weight estimation by automated three-dimensional limb volume model in late third trimester compared to two-dimensional model: a cross-sectional prospective observational study. *BMC Pregnancy Childbirth*. 2021;21(1):365. doi:10.1186/s12884-021-03830-5.
17. Santago P, Gage HD. Statistical models of partial volume effect. *IEEE Trans Image Process*. 1995;4(11):1531–40. doi:10.1109/83.469934.
18. Kimbowa A, Pieters A, Tadayon P, Arora I, Gulam S, Pinos A, et al. Advancements in needle visualization enhancement and localization methods in ultrasound: a literature review. *Art Int Surg*. 2024;4(3):149–69. doi:10.20517/ais.2024.20.
19. Zhu M, Salcudean SE. Real-time image-based B-mode ultrasound image simulation of needles using tensor-product interpolation. *IEEE Trans Med Imag*. 2011;30(7):1391–400. doi:10.1109/TMI.2011.2121091.
20. Chatelain P, Krupa A, Marchal M. Real-time needle detection and tracking using a visually servoed 3D ultrasound probe. In: *Proceedings of the 2013 IEEE International Conference on Robotics and Automation*; 2013 May 6–10; Karlsruhe, Germany. doi:10.1109/ICRA.2013.6630795.
21. Zetting O, Fuerst B, Kojcev R, Esposito M, Salehi M, Wein W, et al. Toward real-time 3D ultrasound registration-based visual servoing for interventional navigation. In: *Proceedings of the 2016 IEEE International Conference on Robotics and Automation (ICRA)*; 2016 May 16–21; Stockholm, Sweden. doi:10.1109/ICRA.2016.7487226.
22. Kallem V, Cowan NJ. Image-guided control of flexible bevel-tip needles. In: *Proceedings of the 2007 IEEE International Conference on Robotics and Automation*; 2007 Apr 10–14; Rome, Italy. doi:10.1109/ROBOT.2007.363930.
23. Baker C, Xochicale M, Joubert F, Lin FY, Mathews S, Shakir DI, et al. Real-time ultrasonic tracking of an intraoperative needle tip with integrated fibre-optic hydrophone. In: *Proceedings of the 2021 IEEE International Ultrasonics Symposium (IUS)*; 2021 Sep 11–16; Xi'an, China. doi:10.1109/ius52206.2021.9593381.
24. Mathiassen K, Dall'Alba D, Muradore R, Fiorini P, Elle OJ. Robust real-time needle tracking in 2-D ultrasound images using statistical filtering. *IEEE Trans Control Syst Technol*. 2017;25(3):966–78. doi:10.1109/tcst.2016.2587733.
25. Agarwal N, Yadav AK, Gupta A, Orlando MF. Real-time needle tip localization in 2D ultrasound images using Kalman filter. In: *Proceedings of the 2019 IEEE/ASME International Conference on Advanced Intelligent Mechatronics (AIM)*; 2019 Jul 8–12; Hong Kong, China. doi:10.1109/aim.2019.8868799.
26. Yan W, Ding Q, Chen J, Liu Y, Cheng SS. Needle tip tracking in 2D ultrasound based on improved compressive tracking and adaptive Kalman filter. *IEEE Robot Autom Lett*. 2021;6(2):3224–31. doi:10.1109/LRA.2021.3063058.
27. Mathews SJ, Shakir DI, Mosse CA, Xia W, Zhang EZ, Beard PC, et al. Ultrasonic needle tracking with dynamic electronic focusing. *Ultrasound Med Biol*. 2022;48(3):520–9. doi:10.1016/j.ultrasmedbio.2021.11.008.
28. Che H, Qin J, Chen Y, Ji Z, Yan Y, Yang J, et al. Improving needle tip tracking and detection in ultrasound-based navigation system using deep learning-enabled approach. *IEEE J Biomed Health Inform*. 2024;28(5):2930–42. doi:10.1109/JBHI.2024.3353343.
29. Hui X, Rajendran P, Ling T, Dai X, Xing L, Pramanik M. Ultrasound-guided needle tracking with deep learning: a novel approach with photoacoustic ground truth. *Photoacoustics*. 2023;34(9):100575. doi:10.1016/j.pacs.2023.100575.

30. Yan W, Ding Q, Chen J, Yan K, Tang RS, Cheng SS. Learning-based needle tip tracking in 2D ultrasound by fusing visual tracking and motion prediction. *Med Image Anal.* 2023;88(6):102847. doi:10.1016/j.media.2023.102847.
31. Khodarahmi M, Maihami V. A review on Kalman filter models. *Arch Comput Meth Eng.* 2023;30(1):727–47. doi:10.1007/s11831-022-09815-7.
32. Garpinger O, Hägglund T, Åström KJ. Performance and robustness trade-offs in PID control. *J Process Control.* 2014;24(5):568–77. doi:10.1016/j.jprocont.2014.02.020.
33. Vrooijink GJ, Abayazid M, Misra S. Real-time three-dimensional flexible needle tracking using two-dimensional ultrasound. In: *Proceedings of the 2013 IEEE International Conference on Robotics and Automation*; 2013 May 6–10; Karlsruhe, Germany.
34. Beigi P, Salcudean SE, Ng GC, Rohling R. Enhancement of needle visualization and localization in ultrasound. *Int J Comput Assist Radiol Surg.* 2021;16(1):169–78. doi:10.1007/s11548-020-02227-7.
35. Cheng Z, Koskinopoulou M, Bano S, Stoyanov D, Rajeeth Savarimuthu T, Mattos LS. Sensing technologies for guidance during needle-based interventions. *IEEE Trans Instrum Meas.* 2024;73(1):4009615. doi:10.1109/TIM.2024.3441017.